FLUTTER SOLUTION OF THE NASA BENCHMARK SUPERCRITICAL WING USING LINEAR AND NON-LINEAR METHODS

Giampaolo Pagliuca[1], José Nicolás Berberoff Naval[1], Matt Forster[1]

[1]BAE Systems Air - Computational Engineering
Filton, Bristol, BS34 7QW, United Kingdom
giampaolo.pagliuca@baesystems.com

Keywords: Aeroelasticity, Flutter, NASA Benchmark Supercritical Wing (BSCW), Aeroelastic-prediction workshop 3 (AePW-3), High angle-of-attack (HAWG)

Abstract: This work reports on the results produced for the Aeroelastic Prediction Workshop 3 (AePW-3) using the BAE Systems Corporate CFD Suite as part of the High Angle-of-attack Working Group (HAWG). The reference test case is the NASA Benchmark Supercritical Wing (BSCW) in R-134a at $M = 0.8$ with an angle-of-attack of 5 deg. The aim of the work is to estimate the flutter critical condition using a coupled numerical model composed of high-fidelity computational fluid dynamics and a structural mechanics modal solver. Results from two distinct approaches are provided. The first one relies on a set of time-marching, initial disturbance simulations, where aerodynamics is fully non-linear. Flutter is identified by post-processing the time-histories of the structural degrees-of-freedom with the logarithmic decrement or the matrix-pencil method. The second approach is based on the evaluation of an interaction matrix Q which links (linearly) a change in the aerodynamic forces to a change in the structural degrees-of-freedom. Such matrix is computed with linearised methods, specifically the linearised frequency domain (LFD) and the pulse-excitation method. The flutter condition is then obtained with the P-K method and using the Q matrix. Steady-state RANS equations with the SA turbulence model were employed to compute the aeroelastic trimmed solutions. Such equilibrium conditions were then used as starting point for all URANS simulations and as linearisation points for the LFD and the pulse-excitation methods. Regarding the linearised methods, the effects of the linearisation point on the final flutter results were investigated. Overall, the flutter results presented in this paper confirm the preliminary data available in literature for both non-linear and linearised methods.

1 INTRODUCTION

Accuracy and a short time-to-solution are crucial for flutter simulations in the long-term vision of the digital twin concept [1]. The accuracy requirement can be met by using Computational Fluid Dynamics (CFD) for the evaluation of aerodynamic loads and Computational Structural Mechanics (CSM) for the structural dynamics. Thus, the coupled CFD-CSM model represents the state-of-the-art for the estimation of the flutter envelope. In short, its most accurate implementation is based on time-marching unsteady simulations with a continuous exchange of information between the non-linear CFD and non-linear CSM solvers. Although this approach represents a valid tool for all flow conditions, a reduction in computational cost (and complexity) of the flutter analysis can be achieved with some linearisations. The first one is usually performed on the CSM side since a modal formulation is often sufficient for structural

dynamics [2]. This leads to a CFD-CSM model composed of a fully non-linear CFD solver and a modal (i.e. linearised) CSM solver. This approach will be referred to as non-linear method hereafter and it has been successfully used to predict the flutter envelope of well-known aeroelastic test cases [3]. A second linearisation can be performed on the CFD side around an equilibrium condition. The idea is to summarise the fluid-structure interaction with a frequency-dependant interaction matrix, Q. Each complex-valued entry of Q links (linearly) a change in one structural degree-of-freedom (d.o.f.) to a variation of one component of the aerodynamic force at a specific oscillation frequency. Two methods are employed in this work to compute Q. The first one, called Linearised Frequency Domain (LFD) [4], is based on the linearisation of the flow equations around an equilibrium condition and the translation of the resulting linear system into frequency-domain. In this way, the entries of Q are obtained directly in frequency-domain. Another approach is to sample, in turn, the system's d.o.f. with a pulse-excitation in time-domain. The entries of Q are computed with a Discrete Fourier Transformation (DFT) from the time-domain histories of the input (i.e. pulse-excitation for one d.o.f.) and the outputs (i.e. components of the aerodynamic force). Once the matrix Q is populated using either of methods, the flutter condition is identified with the P-K method [5].

In this work, the non-linear approach and the two linearised methods (LFD and pulse-excitation) are applied to the flutter analysis of the NASA Benchmark Supercritical Wing (BSCW) as part of the Aeroelastic Prediction Workshop 3 (AePW-3), High Angle-of-attack Working Group (HAWG) [17]. In the next Section 2, a quick description of the numerical methods is given. Section 3 reports on the results from the flutter analysis and an additional investigation on the spacial and temporal discretisation. Conclusions are given in Section 4.

2 NUMERICAL METHODS

The mathematical formulation of the aeroelastic model used in this paper is now derived. Structural equations are written as a first order ordinary differential equation in time t,

$$\frac{\mathrm{d}\mathbf{w}_s}{\mathrm{d}t} = \mathbf{R}_s(\mathbf{w}_f, \mathbf{w}_s) \tag{1}$$

where $\mathbf{w}_s$ is the vector containing the n_s structural unknowns, $\mathbf{R}_s$ is the structural non-linear residual function and $\mathbf{w}_f$ contains the fluid unknowns. The residual function $\mathbf{R}_s$ is split in two terms,

$$\mathbf{R}_s(\mathbf{w}_f, \mathbf{w}_s) = \mathbf{f}_s(\mathbf{w}_s) + \mathbf{f}_a(\mathbf{w}_f, \mathbf{w}_s) \tag{2}$$

where $\mathbf{f}_s$ provides the influence of the structural dynamics on the structural residual and $\mathbf{f}_a$ accounts for external forces, e.g. aerodynamic forces, acting on the structure.

When a modal formulation with m modes is adopted [2], the vector $\mathbf{w}_s$ of structural unknowns contains both the generalised coordinates $\eta = [\eta_1 \ldots \eta_m]^T$ and their corresponding time-derivatives $\dot{\eta} = \frac{\mathrm{d}\eta}{\mathrm{d}t}$, specifically $\mathbf{w}_s = [\eta^T, \dot{\eta}^T]^T$. Thus, the size of the structural problem is $n_s = 2m$. The function $\mathbf{f}_s$ is then defined as

$$\mathbf{f}_s(\mathbf{w}_s) = \begin{pmatrix} 0 & I \\ M^{-1}K & M^{-1}C \end{pmatrix} \begin{bmatrix} \eta \\ \dot{\eta} \end{bmatrix} \tag{3}$$

The matrices M, K and C are the generalised mass, stiffness and damping matrices, respectively, and I is the identity matrix. Regarding the term $\mathbf{f}_a$, it contains the vector of generalised aerodynamic forces (GAFs), i.e. the projection of the aerodynamic forces on the modal shapes.

The non-linear aerodynamic equations are similarly written in a semi-discrete form as

$$\frac{\mathrm{d}\mathbf{w}_f}{\mathrm{d}t} = \mathbf{R}_f(\mathbf{w}_f, \mathbf{w}_s) \tag{4}$$

where $\mathbf{R}_f$ is the non-linear residual function corresponding to the fluid unknowns. The coupled system of aerodynamic and structure is then written as

$$\frac{\mathrm{d}\mathbf{w}}{\mathrm{d}t} = \mathbf{R}(\mathbf{w}_f, \mathbf{w}_s) = \mathbf{R}(\mathbf{w}) \tag{5}$$

by defining the vector $\mathbf{w} = \left[\mathbf{w}_f^T, \mathbf{w}_s^T\right]^T$ and $\mathbf{R}$ is the corresponding non-linear residual function. The total number of unknowns is $n = n_f + n_s$ where n_f is the number of fluid unknowns.

In this work the aerodynamic forces in Eq. (4) are computed using CFD and the CSM in Eq. (1) is implemented using the modal approach. Although the structure is modelled linearly, non-linear phenomena such as the interaction between shock-wave and boundary-layer are fully captured by Eq. (5).

The integration of Eq. (5) in time is referred to as non-linear CFD-CSM and a two-step procedure is required to identify the flutter point with such tool. Firstly, an unsteady simulation is performed for which Eq. (5) is integrated in time. At the beginning of the simulation an initial disturbance in the generalised velocity of the modes is prescribed to enhance any instability of the system. Second, when the simulation is finished, the resulting time-histories of the generalised coordinates are post-processed with either of the logarithmic-decrement (log-dec) [7] or matrix-pencil [8] method to compute the damping. A converging/neutral/diverging time-history corresponds to a positive/zero/negative damping value, respectively, with a diverging curve hinting at the presence of flutter. When results from multiple initial disturbance analyses are available, the damping value can be computed for each simulation. The zero damping condition is then easily found by interpolation.

2.1 Flutter identification with linearised methods

Integrating Eq. (5) in time-domain can be computationally expensive for real-world models. An alternative to reduce the computational cost is to solve the small-sized flutter problem in frequency-domain with the P-K method [5]. Specifically, the flutter equation to solve is

$$\left(M\lambda^2 + K + C\lambda - Q\right)\hat{\mathbf{w}}_s = 0 \tag{6}$$

where $\hat{\mathbf{w}}_s$ is the frequency-domain translation of the structural vector $\mathbf{w}_s$. The matrix $\mathbf{Q}$ is the interaction matrix $Q = \frac{\partial \mathbf{f}_a}{\partial \mathbf{w}_s}$ that relates the generalised aerodynamic forces $\mathbf{f}_a$ to the structural d.o.f. $\mathbf{w}_s$. Computing Q is the computationally expensive part of the linearised methods.

To compute the interaction matrix Q, the pulse excitation method [9] can be used. Starting from an equilibrium condition, a forced-motion unsteady CFD-CSM simulation is performed for each structural degree-of-freedom. The parameters which define the excitation shape and the simulation settings are related to the frequency range of interest [3]. One time-domain simulation is needed for each generalised coordinate, thus exciting one structural d.o.f. at time. An additional drift simulation (i.e. with a non-moving structure) is optionally performed to take into account any deviation of generalised forces from their equilibrium values. Once ready, the time-histories of the generalised forces are post-processed. From each pulse excitation

simulation, one corresponding row in the interaction matrix Q is computed with a Discrete Fourier Transformation.

An alternative method for the computation of Q is the LFD [10, 11]. An equilibrium condition is identified for which the non-linear, residual function of the aerodynamic equation is $\mathbf{R}_f \approx 0$. This is usually the result of a steady-state simulation. In can be shown [3] that linearising the flow equations around this equilibrium condition and assuming an harmonic motion of frequency ω with amplitude $\widehat{\mathbf{w}}_f$ and $\widehat{\mathbf{w}}_s$ for the fluid and structural unknowns, respectively, the LFD equation can be formulated as

$$\left(\frac{\partial \mathbf{R}_f}{\partial \mathbf{w}_f} - i\omega I \right) \widehat{\mathbf{w}}_f = -\frac{\partial \mathbf{R}_f}{\partial \mathbf{w}_s} \widehat{\mathbf{w}}_s \tag{7}$$

Solving Eq. (7) must be performed with iterative methods for real-world test cases. Once the complex-valued flow solution $\widehat{\mathbf{w}}_f$ is computed, one column Q_k of the interaction matrix $Q = [Q_1, \ldots, Q_k, \ldots Q_m]$ relating the generalised aerodynamic forces $\mathbf{f}_a$ to the structural degrees-of-freedom is obtained with the chain rule

$$Q_k = \frac{\partial \mathbf{f}_a}{\partial \mathbf{w}_f} \frac{\partial \mathbf{w}_f}{\partial \mathbf{w}_s} = \frac{\partial \mathbf{f}_a}{\partial \mathbf{w}_f} \widehat{\mathbf{w}}_f \tag{8}$$

2.2 Computational methods

Simulations were performed using the BAE Systems Corporate CFD Suite, known as Solar and Flare [12, 13], which includes a mesh generator, CFD solver and an aeroelastic toolkit. The aeroelastic toolkit is composed of: a mode shape mapping utility, a CSM solver as well as an LFD solver. Regarding the CFD solver, a cell-centred, finite-volume approach is used to integrate Eq. (4) for inviscid or viscous flows. A fully implicit scheme is employed for steady-state computations and for the inner iterations of unsteady loops. Time integration is performed with a high order Runge-Kutta scheme. The CSM solver used for this work is based on the modal decomposition of structural deformations [2]. The structural equations are integrated with the β-Newmark scheme [14]. The coupling between the CFD solver and the CSM solver is performed at each time-step (loosely-coupled approach) with the possibility of running multiple CSM inner iterations (strongly-coupled approach). The aerodynamic loads coming from the CFD solver are used by the CSM solver to compute the up-to-date values of the generalised coordinates. The deformation of the CFD surface mesh is the linear combination of the mode shapes scaled by their corresponding generalised coordinate. Volume mesh deformation is performed with Radial Basis Function (RBF) interpolation [15].

The LFD solver uses a second-order Jacobian matrix obtained with automatic differentiation. The right-hand side vector $\frac{\partial \mathbf{R}_f}{\partial \mathbf{w}_s}$ is computed with central finite differences. The system is preconditioned with a first-order Jacobian matrix. The linear system is solved using the sparse, iterative linear solvers available in PETSc [16].

3 RESULTS

Numerical results are reported for the NASA Benchmark Supercritical wing for which the CAD geometry, structural model and experimental data is available in literature [17]. The aim is to identify the flutter point (i.e. critical value of dynamic pressure) for the wing at $M = 0.8$ with an angle-of-attack of $5 \deg$, using R-134a gas as a fluid medium. The specific flow conditions investigated in this work are summarised in Tab. (1) with imperial units. Regarding the structural

	Case 1	Case 2	Case 3	Case 4	Case 5	Case 6	Case 7	Case 8	Case 9	Case 10	Case 11	Case 12	Case 13
M	0.799	0.800	0.800	0.800	0.800	0.800	0.800	0.800	0.800	0.800	0.800	0.801	0.801
$q\,[\mathrm{psf}]$	10.02	25.00	35.00	50.00	75.00	100.00	134.00	143.00	152.00	168.80	200.00	225.00	250.00
Re	237461	592224	829213	1184801	1777732	2371336	3178880	3392751	3606668	4006103	4748658	5343835	5939368
$Re_c\,[1/\mathrm{ft}]$	178096	444168	621910	888601	1333299	1778502	2384160	2544563	2705001	3004577	3561493	4007876	4454526
$V\,[\mathrm{ft/s}]$	440.45	440.63	440.59	440.51	440.39	440.21	440.05	440.00	439.96	439.88	439.70	439.58	439.46
$a\,[\mathrm{ft/s}]$	551.08	550.94	550.85	550.71	550.48	550.25	549.94	549.86	549.78	549.62	549.34	549.11	548.88
$T_{stat}\,[\mathrm{°F}]$	80.87	80.83	80.83	80.82	80.81	80.80	80.78	80.77	80.77	80.76	80.74	80.73	80.71
$\rho\,[\mathrm{slugs/ft^3}]$	0.00010	0.00026	0.00036	0.00052	0.00077	0.00103	0.00138	0.00148	0.00157	0.00175	0.00207	0.00233	0.00259
γ	1.1121	1.1122	1.1123	1.1124	1.1126	1.1128	1.1131	1.1131	1.1132	1.1133	1.1136	1.1138	1.1139
$\mu\,[\mathrm{lb \cdot s/ft^2}]$	2.555E-07	2.555E-07	2.555E-07	2.555E-07	2.555E-07	2.555E-07	2.554E-07	2.554E-07	2.554E-07	2.554E-07	2.554E-07	2.554E-07	2.55E-07
Pr	0.6839	0.6840	0.6841	0.6842	0.6844	0.6845	0.6847	0.6848	0.6848	0.6849	0.6851	0.6853	0.6854
$P_{tot}\,[\mathrm{psf}]$	40.00	99.72	139.61	199.45	299.18	399.00	534.69	570.61	606.53	673.59	798.21	898.01	997.83
$P_{stat}\,[\mathrm{psf}]$	28.207	70.319	98.449	140.644	210.975	281.366	377.050	402.380	427.711	474.996	562.873	633.255	703.643
$T_{stag}\,[\mathrm{°F}]$	100	100	100	100	100	100	100	100	100	100	100	100	100

Table 1: Flow conditions for the flutter analysis. The dynamic pressure ranges from $10\,\mathrm{psf}$ to $250\,\mathrm{psf}$ whereas the angle-of-attack is $5\,\mathrm{deg}$ for all flow conditions.

Discretisation	Scaling	Mesh size (Million)
Level 1	4.00	0.77
Level 2	2.00	3.13
Level 3	1.25	10.90
Level 4	1.10	12.82
Level 5	1.00	14.77
Level 6	1/1.10	36.67
Level 7	1/1.25	40.47
Level 8	1/2.00	81.02

Table 2: Family of meshes for the mesh convergence study. Starting from Level 5, a number of 4 coarser meshes and 3 finer meshes were obtained by scaling the target element size.

model, two d.o.f. are considered, specifically vertical translation in the Z direction (heave) and rigid rotation around the Y axis (pitch). The structural model is implemented with a modal formulation and the mode shapes corresponding to heave and pitch were generated using a rigid translation of $1\,\mathrm{m}$ and a rigid rotation of $1\,\mathrm{rad}$, respectively. Values of mass and stiffness were taken from literature for the Pitch And Plunge Apparatus (PAPA) configuration [18]. Note, the splitter plate was modelled as a symmetry plane in all CFD simulations run for this paper.

3.1 Spacial and temporal discretisation

A preliminary mesh convergence study was undertaken. Starting from the CAD geometry, a CFD mesh is obtained with the BAE Systems Corporate CFD Suite in three steps: first, wall surfaces are meshed according to target element sizes provided by the user at distinct locations in the domain; secondly, the boundary layer is grown from the wall surfaces according to the requirements of turbulence model; thirdly, the domain is filled with a Cartesian background mesh. The process is almost completely automatic once the target mesh element size is set at few specific locations. Using some engineering judgement at first, a reference mesh with 14.77×10^6 cells was obtained. From that, a family of 8 meshes was derived by scaling the target element size by a factors of 1.10, 1.25, 2 and 4, as summarised in Tab. (2). Aerodynamic forces and pressure distribution were then computed, in turn, for all meshes in the family by running a steady-state simulation for the flow condition named *Case 6* in Tab. (1) with the SST turbulence model and CFL number of 1.5. Each steady-state simulation run for a fixed number of 80000 iterations during which the density residual decreased to values smaller than 1×10^{-7}. The final values of CF_z (coefficient of aerodynamic force in the vertical direction) is plotted against the discretisation level in Fig. 1(a). Apart from *Level 1*, the maximum difference between the other *Levels 2* to *8* is smaller than 2%. This is confirmed by the pressure distribution on the

(a) Coefficient of force in the vertical direction

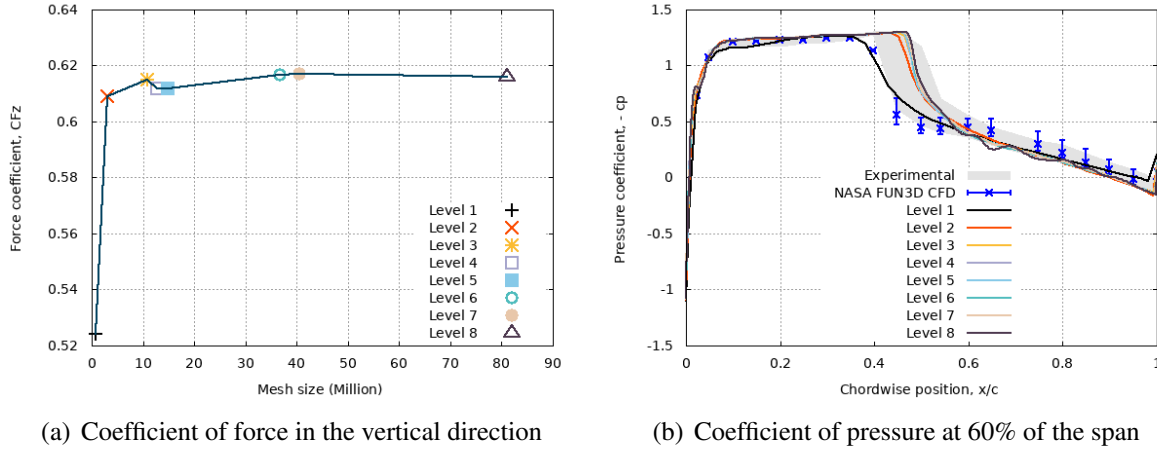(b) Coefficient of pressure at 60% of the span

Figure 1: Mesh convergence study. A steady-state simulation at the same flow condition was performed for all discretisation levels. The assessment was conducted looking at the aerodynamic force in the vertical direction, CF_z and the pressure distribution at 60% of the span.
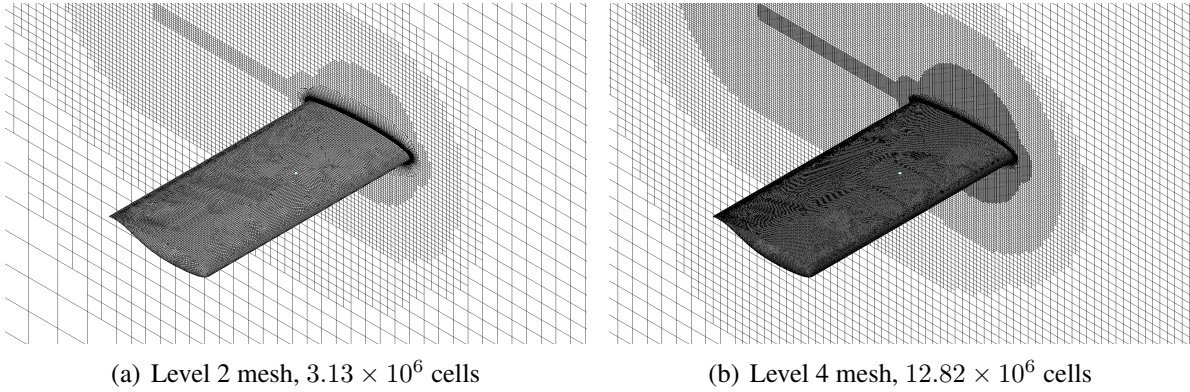

(a) Level 2 mesh, 3.13×10^6 cells

(b) Level 4 mesh, 12.82×10^6 cells

Figure 2: Mesh convergence study. Two meshes were chosen for the aeroelastic analysis, corresponding to *Level 2* and *Level 4* in Tab. (2).

upper surface at 60% of the span in Fig. 1(b) which shows a visible difference between *Level 1* and all other levels. In addition, the pressure distribution from [17] is reported in Fig. 1(b) as well. Although the literature data is from unsteady simulations, it provides a range over which the pressure distribution is expected. As a result of the mesh convergence study, two meshes were chosen for the subsequent simulations, specifically *Level 2* and *Level 4* with 3.13×10^6 and 12.82×10^6 cells, respectively. The coarse mesh in Fig. 2(a) represents a trade-off between accuracy and computational cost. Thus, it became the preferred choice for the CFD-CSM simulations. The fine mesh in Fig. 2(b) was employed mainly to investigate aerodynamic phenomena when fewer simulations were needed.

The temporal discretisation was investigated next. An unsteady CFD-CSM simulation was performed with the fine mesh for 3 values of time step, specifically $1 \times 10^{-4}\,\text{s}$, $2 \times 10^{-4}\,\text{s}$ and $4 \times 10^{-4}\,\text{s}$, and for a total simulation time of $5\,\text{s}$. The flow condition corresponds to *Case 5* in Tab. (1) and an initial disturbance of 0.1% of the free-stream velocity was prescribed in the velocity of both d.o.f.. Loosely and strongly coupled schemes were investigated for a total of 6 simulations. Note, the key difference between loosely and strongly coupled algorithms lies in the exchange of information (e.g. forces and mesh deformation) between the CFD and CSM solvers. In a loosely coupled scheme, the exchange happens only once for each physical

(a) Heave, whole time-history

(b) Pitch, whole time-history

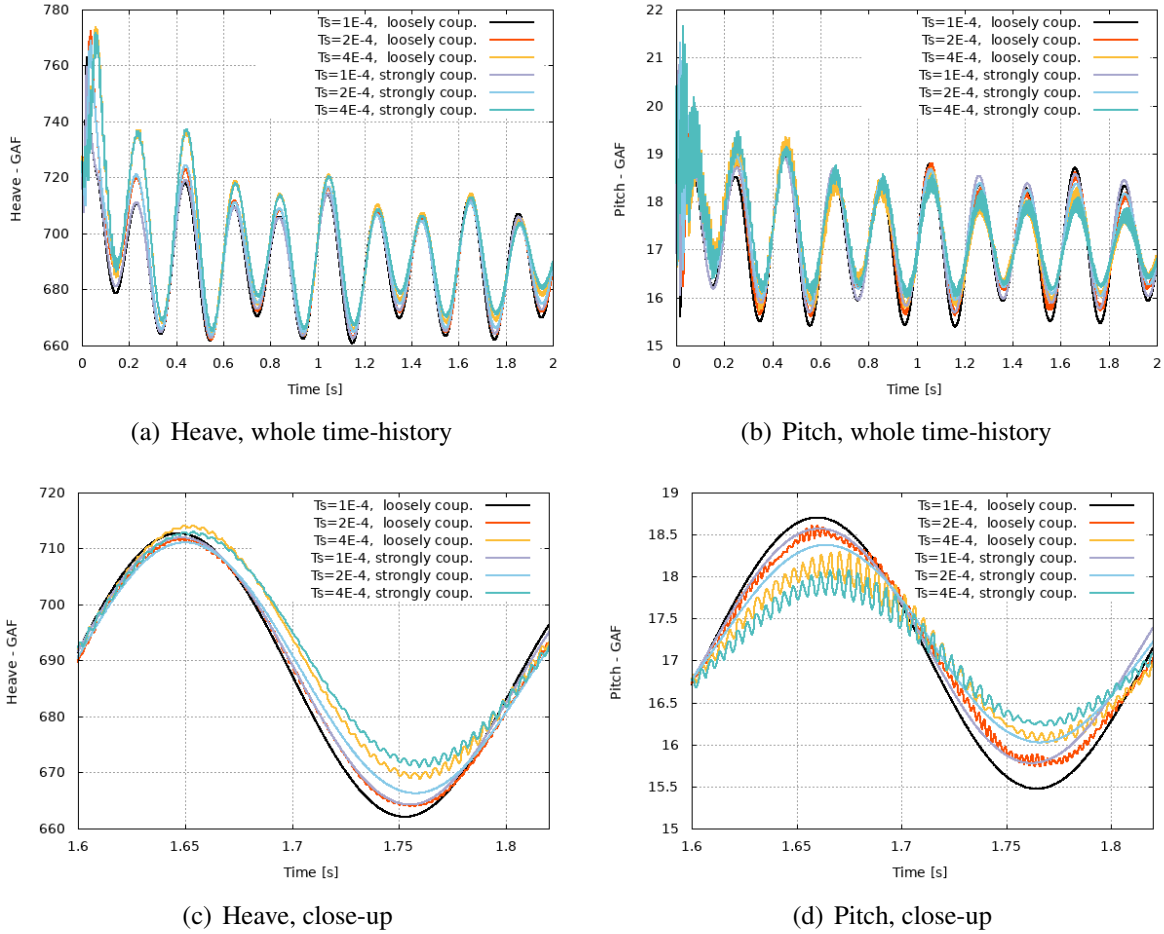(c) Heave, close-up

(d) Pitch, close-up

Figure 3: Time-step analysis. A number of 6 unsteady, initial disturbance CFD-CSM simulations were performed with the same fine mesh, same flow conditions but different time-step and coupling scheme. An overview and a close-up of the GAF time-history are provided for both d.o.f.

time-step whereas in a strongly coupled approach this happens multiple times within the same physical time-step, specifically twice for our simulations. The time-history of the GAFs is depicted in Fig. 3 for both d.o.f.. Looking at Fig. 3(a) and Fig. 3(b), it is clear that all loosely coupled simulations capture the system's response in terms of oscillation frequency but the larger time-steps (2×10^{-4} s and 4×10^{-4} s) produce secondary oscillations. This is particularly clear from Fig. 3(c) and Fig. 3(d). Regarding the strongly coupled simulations, both time-steps 1×10^{-4} s and 2×10^{-4} s provide a smooth response curves. Overall, the time-step analysis was unable to identify a converged time-step value and further investigation is needed in that direction. However, the largest relative difference in the GAF responses was found around 1.65 s for the pitch d.o.f. as shown in Fig. 3(d) and it is quantified in 5% with respect to the strongly coupled smallest time-step. Considering only time-steps that provide a smooth response for both d.o.f., this difference is down to less than 3%. Thus, a time-step of 2×10^{-4} s with a strongly coupled scheme represents a trade-off between computational cost and accuracy.

3.2 Flutter analysis with linearised methods

The flutter point was first computed with the LFD solver. The steady-state solution needed to perform the flow linearisation was obtained with a static aeroelastic trimming. In practice, a steady-state coupled CFD-CSM simulation was run with the coarse mesh and the SA turbulence model. Every 500 CFD iterations, 1 coupled CFD-CSM iteration was performed to update

(a) Magnitude of the entry $Q_{24} = CFz_\theta$
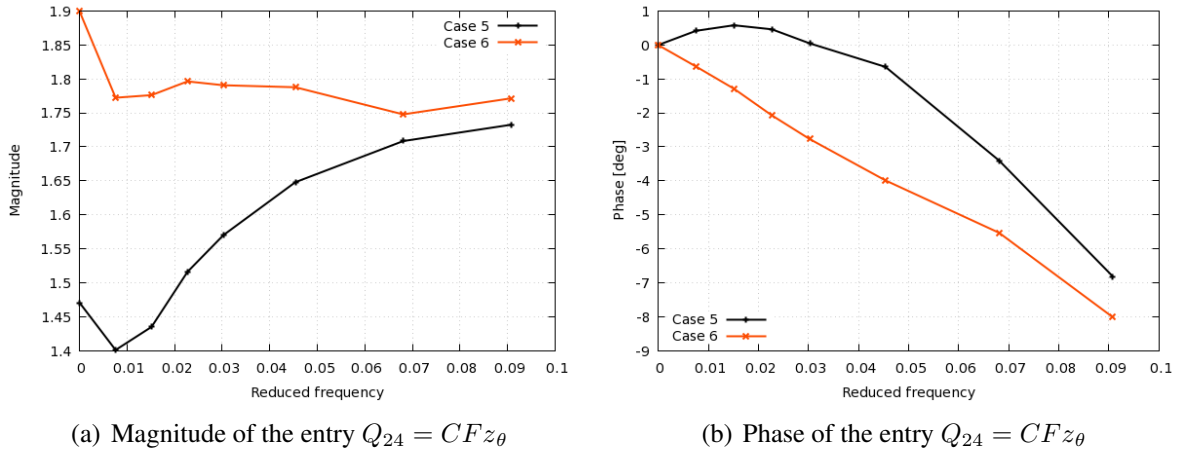
(b) Phase of the entry $Q_{24} = CFz_\theta$

Figure 4: The dynamic derivative $Q_{24} = CFz_\theta$ was computed with the LFD at 2 distinct flow conditions to highlight the influence of the linearisation point on the entries of Q.

the wing position in terms of heave translation and pitch rotation. An artificial damping of $250\,\mathrm{N\,s/\,m}$ was added to structural model to speed-up the trimming process which converged in less than 80 coupled CFD-CSM iterations. Two results were obtained: the equilibrium position of the wing (i.e. non-zero vertical translation and non-zero pitch rotation) and the corresponding flow solution. The LFD solver was then restarted from the aeroelastic trimmed solution and the dynamic derivatives were computed at 8 frequencies, specifically $0\,\mathrm{rad/\,s}$, $5\,\mathrm{rad/\,s}$, $10\,\mathrm{rad/\,s}$, $15\,\mathrm{rad/\,s}$, $20\,\mathrm{rad/\,s}$, $30\,\mathrm{rad/\,s}$, $45\,\mathrm{rad/\,s}$ and $60\,\mathrm{rad/\,s}$. The entries of the matrix Q in Eq. (6) were eventually computed with Eq. (8).

Although the LFD needs only one linearisation point, the whole process was repeated for 2 flow conditions (*Case 5* and *6*). The objective was to investigate the effects of the linearisation point on the dynamic derivatives and the evaluation of the flutter point. The representative entry Q_{24} of Q, which links a change in the pitch rotation to a change in the vertical force, is shown in Fig. 4. Taking *Case 6* as reference, the relative error at frequency 0 in terms of magnitude (Fig. 4(a)) is -22% with respect to *Case 5*. At the largest value of reduced frequency, the relative error becomes smaller (-3.3%). When it comes to Fig. 4(b), the phase at frequency 0 is 0 for all flow conditions, as expected from theory. A relative error of -12% was found between *Case 6* and *Case 5* at the largest value of reduced frequency.

Once the entries of the matrix Q are available, the flutter equation (6) can be solved with a tracing algorithm based on Newton's method [19]. As a result, the evolution of the two eigenvalues (one for each d.o.f.) of Eq. (6) is shown in Fig. 5 with respect to the dynamic pressure. The heave mode is always stable as visible in Fig. 5(a). Conversely, the pitch mode evolves into flutter when a critical value of dynamic pressure q^* is reached. The specific value of q^* depends on the flow condition at which the dynamic derivatives were computed. It was found that $q^* = 253\,\mathrm{psf}$ for *Case 6* and $q^* = 303\,\mathrm{psf}$ for *Case 5*. Regarding the flutter frequency in Fig. 5(b), the two flow conditions lead to very similar values in the range $[4.3, 4.6]\,\mathrm{Hz}$. The flutter point obtained with the LFD closely resemble the preliminary result provided in [17] and computed with an adaptive version of the LFD.

The matrix Q was computed with the pulse-excitation method for *Case 6* and *5* as well, using the coarse mesh and the SA turbulence model. Each d.o.f. was excited individually by means of a forced-motion unsteady simulation. The input signal was built according to the guidelines

8

(a) Real part of the eigenvalue, $\mathrm{Re}\,(\lambda)$

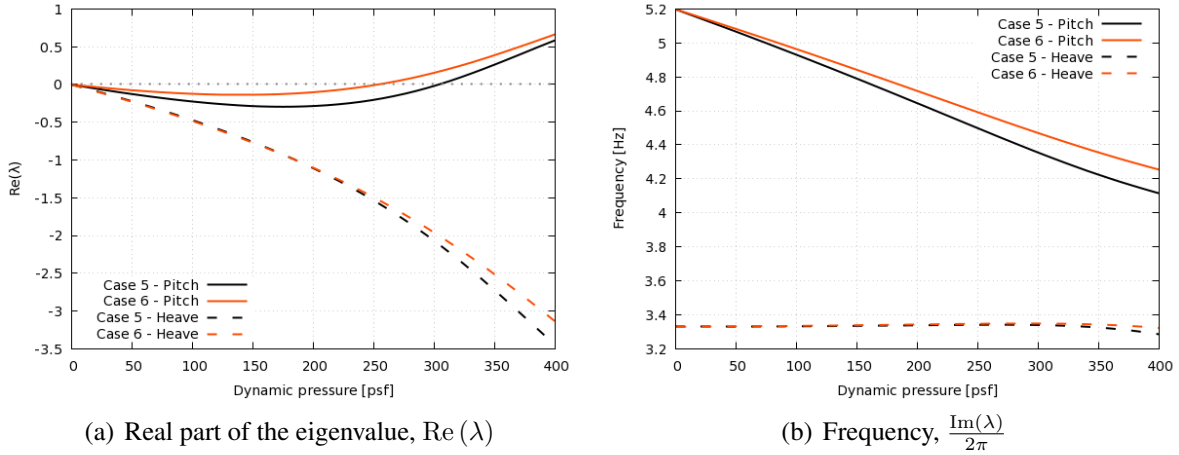(b) Frequency, $\frac{\mathrm{Im}(\lambda)}{2\pi}$
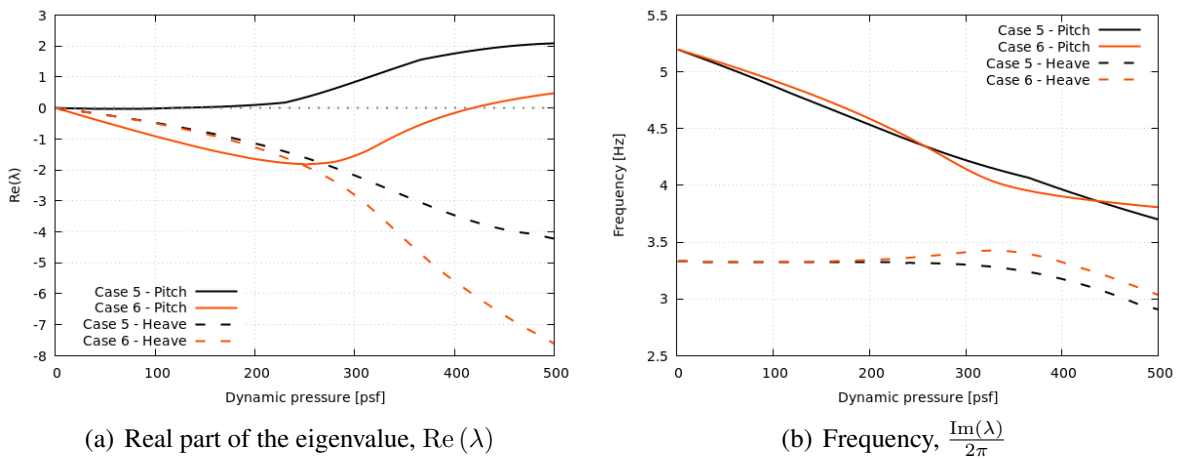
Figure 5: Flutter analysis with the LFD method. Plots of the eigenvalues of Eq. (6) with respect to dynamic pressure. The pitch mode becomes unstable at $253\,\mathrm{psf}$ for *Case 6*, $303\,\mathrm{psf}$ for *Case 5*.

(a) Real part of the eigenvalue, $\mathrm{Re}\,(\lambda)$

(b) Frequency, $\frac{\mathrm{Im}(\lambda)}{2\pi}$

Figure 6: Flutter analysis with the pulse-excitation method. Plots of the eigenvalues of Eq. (6) with respect to dynamic pressure. The pitch mode becomes unstable at $418\,\mathrm{psf}$ for *Case 6*, $118\,\mathrm{psf}$ for *Case 5*.

provided in [3] to excite the frequency range between 0 and $20\,\mathrm{Hz}$. In practice, the total simulation time is $10\,\mathrm{s}$, the time-step is $0.001\,\mathrm{s}$, the pulse has a duration of $0.25\,\mathrm{s}$ and an amplitude of 0.001 with its peak located at 30% of its duration. The unsteady simulations (one for each d.o.f.) were restarted from the static aeroelastic trimmed solution, which was already available from the LFD study, and the input signal was added to the baseline initial deformation. A number of 50 CFD iterations were run for each physical time-step. In addition to the two pulse-excitation simulations, a drift simulation was performed as well with the same time discretisation and restart parameters to account for any deviation of the aerodynamic forces from their equilibrium values. Once the time-histories of the aerodynamic forces were available, the entries of Q were computed with a DFT, as described in 2. Subsequently, the flutter equation was solved following the same steps already described in the previous paragraph for the LFD and the resulting plots are shown in Fig. 6. The heave d.o.f. is stable whereas flutter occurs in the pitch d.o.f. at $418\,\mathrm{psf}$ for *Case 6* and $118\,\mathrm{psf}$ for *Case 5* as reported in Fig. 6(a). Regarding the flutter frequency, it is evaluated at $3.89\,\mathrm{Hz}$ and $4.81\,\mathrm{Hz}$, respectively. Thus, the flutter points computed with the LFD solver and the pulse-excitation method differ in terms of dynamic pressure. However, both sets of results are within the range of dynamic pressure expected from linearised methods for this specific test case. The difference might be due to linearisation pro-
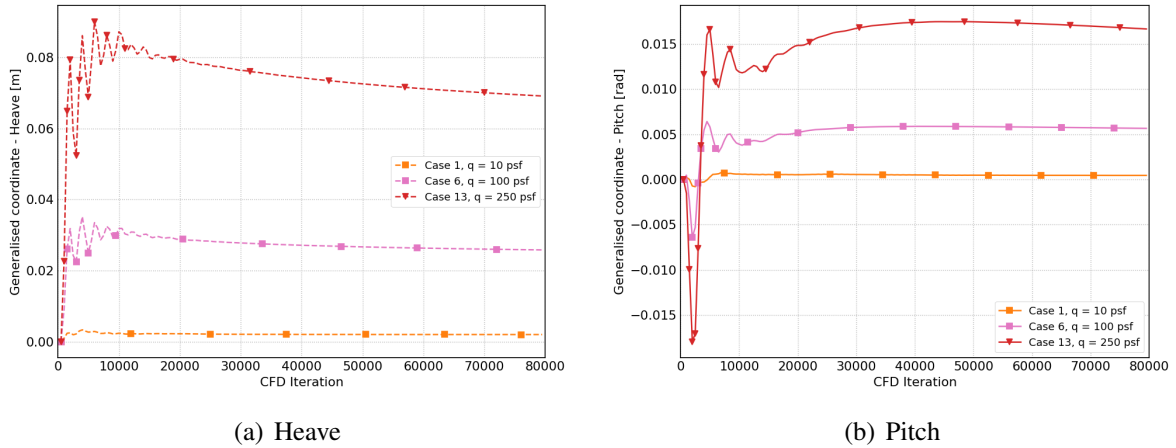
(a) Heave

(b) Pitch

Figure 7: Evolution of the generalised coordinates during the static aeroelastic trimming for 3 flow conditions (*Case 3*, *6* and *13*). The trimming process was repeated for all flow conditions in Tab. (1).

cess which should exclude any non-linear effect. An investigation, for example into the pulse amplitude, is needed.

3.3 Flutter analysis with the non-linear CFD-CSM

The non-linear method described in Section 2 was employed next to evaluate the flutter point. For all flow conditions in Tab. (1), the static aeroelastic trimming process, described at the beginning of Section 3.2, was performed with the coarse mesh and the SA turbulence model. In Fig. 7 the evolution of the generalised coordinates towards the aeroelastic equilibrium is shown for 3 flow conditions. The static aeroelastic trimmed solution was the basis to restart an unsteady, coupled CFD-CSM simulation with a total simulation time of $5\,\mathrm{s}$. The time discretisation parameters for the unsteady CFD-CSM simulation were chosen according to the results presented in Section 3.1, specifically a strongly coupled scheme with a total of 50 CFD subiterations split in 2 CFD-CSM iterations for each physical time-step and a time-step of $2 \times 10^{-4}\,\mathrm{s}$ was employed. An initial disturbance of 0.1% of the free-stream velocity was prescribed in the velocity of both d.o.f. to speed-up the development of the response towards a stable (or unstable) behaviour. The time-histories of the generalised velocities for *Case 4*, *5* and *6* are shown in Fig. 8 as an example. The heave d.o.f. was found to be stable for all flow conditions and a subset of the available results is shown in Fig. 8(a). More interesting is the behaviour of the pitch d.o.f. in Fig. 8(b) since its response is stable for values of dynamic pressure up to $50\,\mathrm{psf}$ (*Case 4*) and it becomes unstable at $75\,\mathrm{psf}$ (*Case 5*) and $100\,\mathrm{psf}$ (*Case 6*).

The results of the unsteady simulations were analysed with the logarithmic-decrement (log-dec) algorithm and the matrix-pencil method. During the post-processing, it was found both methods can provide a wrong estimation of the damping when applied to oscillations which occur around a time-dependent reference value. In practice, that is the case of the generalised coordinates which, starting from the initial value computed with the trimming process, can develop a slightly different equilibrium towards the end of the unsteady simulation because of more converged aerodynamic forces. A possible workaround to obtain a more robust formulation was to post-process the generalised velocity instead since it can be safely assumed that the velocity value at the equilibrium is zero. For the log-dec, only data from the last 15 periods were taken into account in order to deal with an almost non-periodic response in the heave d.o.f. for *Case 7* and above, as reported in the following paragraph. Regarding the matrix-pencil, its input signal was downsampled to 300 data points to speed-up the computations. Damping and frequency
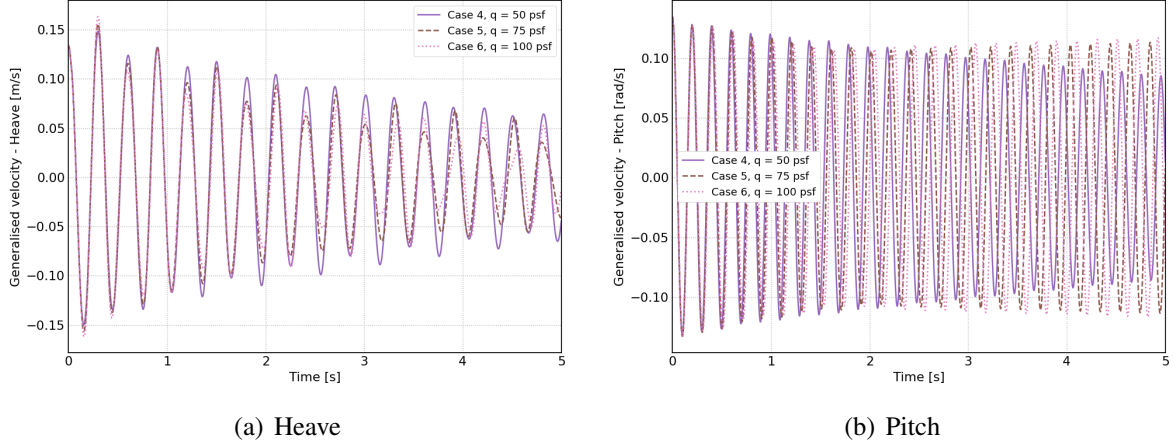
10

(a) Heave

(b) Pitch

Figure 8: Time-histories of the generalised velocities from 3 unsteady, coupled CFD-CSM simulations. The system's response in the heave d.o.f. is always stable whereas an unstable behaviour was found for pitch at $75\,\mathrm{psf}$ (*Case 5*) and $100\,\mathrm{psf}$ (*Case 6*).
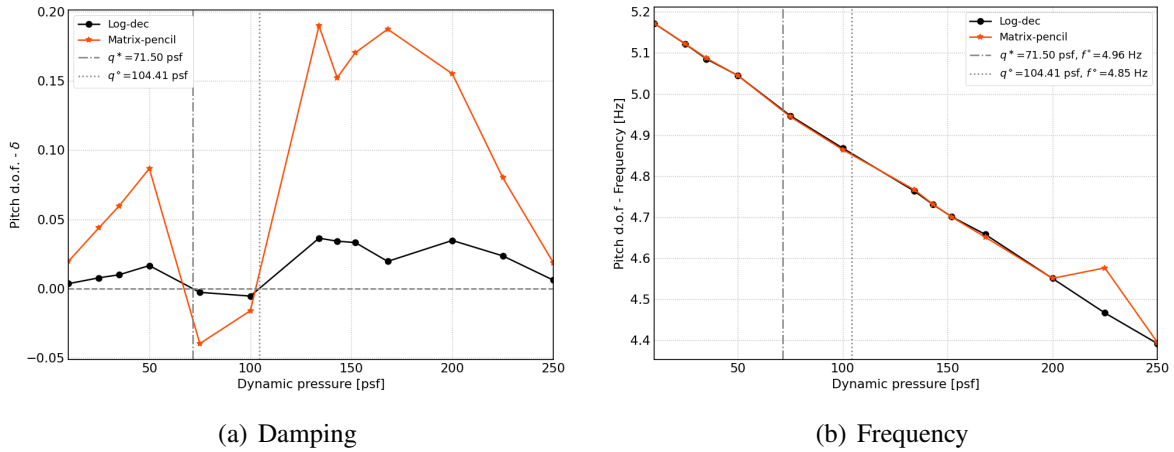

(a) Damping

(b) Frequency

Figure 9: Damping and frequency plotted against dynamic pressure. Log-dec algorithm was applied to the last 15 periods of the generalised velocities. Linear interpolation between the data points was used to compute the crossings at q^* and $q^\diamond$.

results are given in Fig. 9(a) and Fig. 9(b). Only plots for the pitch d.o.f. are reported for sake of conciseness since the damping of the heave d.o.f. was positive (stable) for all flow conditions. Applying linear interpolation between the data points, two crossings q^* and $q^\diamond$ of the horizontal axis were identified for the pitch d.o.f.. Note, the specific values of q^* and $q^\diamond$ were estimated with both log-dec and matrix-pencil method and their results differ by less than 4%. So, only the numerical values from the log-dec are reported hereafter. The first crossing, which is assumed to be the critical value for flutter, is at $q^* = 71.5\,\mathrm{psf}$. For values of dynamic pressure q where $q < q^*$, the system's behaviour is stable. The second crossing is located at $q^\diamond = 104.41\,\mathrm{psf}$ and the pitch response is unstable for $q^* < q < q^\diamond$. For $q > q^\diamond$, the behaviour becomes stable again as shown with the time-histories in Fig. 10. Comparing Fig. 8 with Fig. 10, it is interesting to notice that the pitch responses for $q < q^*$ and $q > q^\diamond$ look similar, i.e. a damped oscillation. However, the time-history of the heave d.o.f., which is initially a damped oscillation for $q < q^*$, evolves in an almost non-periodic signal when $q > q^\diamond$.

To further investigate on that, an additional unsteady simulation was performed with the fine mesh and the SST turbulence model for *Case 6*. The static aeroelastic trimming is first per-
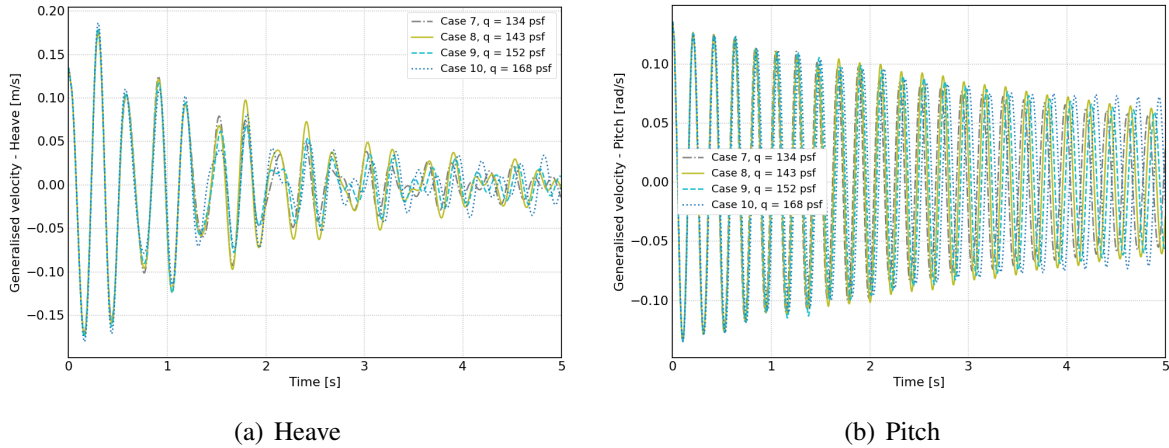
(a) Heave

(b) Pitch

Figure 10: Time-histories of the generalised velocities from the unsteady, coupled CFD-CSM simulations run for *Case 7 to 10*. Although the system's response is stable for both d.o.f., the time-histories of the heave generalised velocity looks more and more aperiodic with an increasing value of q.
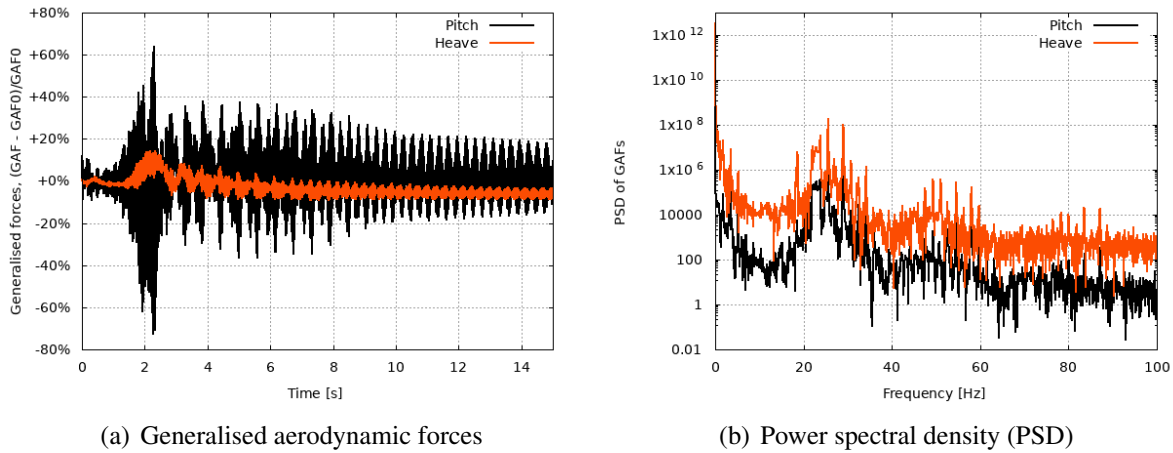

(a) Generalised aerodynamic forces

(b) Power spectral density (PSD)

Figure 11: Time-history and PSD of the generalised aerodynamic forces for a fluid-only simulations run with the fine mesh and the SST turbulence model for *Case 6*. The values in the time-history are expressed as percent variation from the trimmed solution.

formed to obtain the equilibrium position of the wing. The unsteady simulation is then restarted from the trimmed solution but the structure is kept fixed, not moving, since the objective of the investigation is to obtain insights on the frequency contents of the aerodynamic forces. The simulation was run for a total of $15\,\mathrm{s}$, with a physical time-step of $5 \times 10^{-3}\,\mathrm{s}$ and 50 CFD subiterations per time-step. The time-history of the generalised forces is depicted in Fig. 11(a). The system's response for both d.o.f. evolves from an initial transient (from $0\,\mathrm{s}$ to $\approx 10\,\mathrm{s}$) into simple oscillations (from $\approx 10\,\mathrm{s}$ onwards). The corresponding Power Spectral Density (PSD) plots are given in Fig. 11(b) where one interesting region can be identified around $20\,\mathrm{Hz}$, which might correspond to the fundamental frequency reported in the experimental data available in literature [17].

4 CONCLUSIONS

This work reports on the flutter analysis performed on the NASA Benchmark Supercritical Wing using the BAE Systems Corporate CFD Suite as part of the AePW-3 workshop. A 3.13×10^6 cells mesh with the SA turbulence model was employed for the analysis. Linearised methods (i.e. LFD and pulse-excitation) were applied to the static aeroelastic trimmed solution (i.e. the

equilibrium condition that fluid and structure reach with a steady-state assumption). The analysis was repeated for two flow conditions, specifically $q = 75$ psf and $q = 100$ psf, to investigate the effects of the linearisation point on the flutter computations. Both linearised methods provide a critical dynamic pressure for flutter in the range $[120, 420]$ psf involving the pitch d.o.f.. A non-linear approach was pursued as well which required one unsteady, coupled CFD-CSM simulation with an initial disturbance for each flow condition to be investigated. The flutter dynamic pressure was identified by post-processing the time-histories of the generalised velocities. The critical value of dynamic pressure was found at 71.50 psf for the pitch d.o.f.. The difference between linearised and non-linear models seems to suggest a strongly non-linear behaviour of the fluid flow around the linearisation point and a high sensitivity to the linearisation method. An interesting follow-up study might focus on the system's behaviour for higher values of dynamic pressure (e.g. larger than 120 psf) since the results obtained so far suggest a stabilisation of the pitch d.o.f. and a more chaotic response in the heave d.o.f.. Overall, the results presented in this work are aligned with preliminary data available in literature for both linearised and non-linear methods.

5 REFERENCES

[1] BAE Systems (ref: 083/2020, 2020). British engineers reveal digital design concepts to shape next generation of combat aviation. Press release.

[2] Wright, J. and Cooper, J. (2015). *Introduction to aircraft aeroelasticity and loads*. Wiley, 2nd ed.

[3] Pagliuca, G. and Forster, M. (AIAA-2022-1326, 2022). Aeroelastic solutions of the AGARD 445.6 wing using linear- and nonlinear-CFD.

[4] Forster, M. (2019). Developments towards fluid-structure interaction simulations in BAE Systems' corporate CFD suite. In *Aerodynamic Tools and Methods in Aircraft Design*. Royal Aeronautical Society.

[5] Hassig, H. (1971). An approximate true damping solution of the flutter equation by determinant iteration. *Journal of Aircraft*, 8(11), 885–889.

[6] Chwalowski, P., Heeg, J., and Biedron, R. T. (AIAA-2017-0190, 2017). Numerical investigations of the Benchmark Supercritical Wing in transonic flow.

[7] Inman, D. J. (2008). *Engineering vibration (3rd.)*. Pearson Education, Inc.

[8] Kiviaho, J. F., Jacobson, K. E., and Kennedy, G. J. (2019). Flutter boundary identification from time-domain simulations using the matrix pencil method. *AIAA Journal*, 57(8), 3639–3645. doi:10.2514/1.J058072.

[9] Kaiser, C., Thormann, R., Dimitrov, D., et al. (ref: 370189, 2015). Time-linearized analysis of motion-induced and gust-induced airloads with the DLR-TAU code. In *Deutscher Luft- und Raumfahrtkongress*. German Aerospace Center (DLR).

[10] Hall, K. and Crawley, E. (1989). Calculation of unsteady flows in turbomachinery using the linearized Euler equations. *AIAA Journal*, 27(6), 777–787.

[11] Thormann, R. and Widhalm, M. (2013). Linear-frequency-domain predictions of dynamic-response data for viscous transonic flows. *AIAA Journal*, 51(11), 2540–2557.

[12] Martineau, D., Stokes, S., Munday, S., et al. (AIAA-2006-534, 2006). Anisotropic hybrid mesh generation for industrial RANS applications.

[13] Neilson, O. (2015). Automatic differentiation for aerodynamics applications. In *27th International Conference on Parallel Computational Fluid Dynamics - ParCFD 2015*.

[14] Newmark, N. M. (1959). A method of computation for structural dynamics. *Journal of Engineering Mechanics*, 85(3), 67–94.

[15] de Boer, A., van der Schoot, M. S., and Bijl, H. (2007). Mesh deformation based on radial basis function interpolation. *Computers and Structures*, 85(11-14), 784–795.

[16] Abhyankar, S., Brown, J., Constantinescu, E. M., et al. (2018). PETSc/TS: A modern scalable ODE/DAE solver library. *arXiv preprint 1806.01437*.

[17] Chwalowski, P., Massey, S. J., Jacobson, K., et al. (AIAA-2022-1347, 2022). Progress on transonic flutter and shock buffet computations in support of the third Aeroelastic Prediction Workshop.

[18] Heeg, J., Chwalowski, P., Raveh, D. E., et al. (AIAA-2015-0437, 2015). Plans and example results for the 2nd AIAA Aeroelastic Prediction Workshop.

[19] Pagliuca, G. and Timme, S. (AIAA-2016-3850, 2016). Flight dynamics mode identification and model reduction using computational fluid dynamics.

COPYRIGHT STATEMENT